

2D k -th nearest neighbor statistics: a highly informative probe of galaxy clustering

Sihan Yuan^{*}, Alvaro Zamora, and Tom Abel

Kavli Institute for Particle Astrophysics and Cosmology, Stanford University, 452 Lomita Mall, Stanford, CA 94305, USA

Department of Physics, Stanford University, 382 Via Pueblo Mall, Stanford, CA 94305, USA

SLAC National Accelerator Laboratory, 2575 Sand Hill Road, Menlo Park, CA 94025, USA

Accepted XXX. Received YYY; in original form ZZZ

ABSTRACT

Beyond standard summary statistics are necessary to summarize the rich information on non-linear scales in the era of precision galaxy clustering measurements. For the first time, we introduce the 2D k -th nearest neighbor (k NN) statistics as a summary statistic for discrete galaxy fields. This is a direct generalization of the standard 1D k NN by disentangling the projected galaxy distribution from the redshift-space distortion signature along the line-of-sight. We further introduce two different flavors of 2D k NNs that trace different aspects of the galaxy field: the standard flavor which tabulates the distances between galaxies and random query points, and a “DD” flavor that tabulates the distances between galaxies and galaxies. We showcase the 2D k NNs’ strong constraining power both through theoretical arguments and by testing on realistic galaxy mocks. Theoretically, we show that 2D k NNs are computationally efficient and directly generate other statistics such as the popular 2-point correlation function, voids probability function, and counts-in-cell statistics. In a more practical test, we apply the 2D k NN statistics to simulated galaxy mocks that fold in a large range of observational realism and recover parameters of the underlying extended halo occupation distribution (HOD) model that includes velocity bias and galaxy assembly bias. We find unbiased and significantly tighter constraints on all aspects of the HOD model with the 2D k NNs, both compared to the standard 1D k NN, and the classical redshift-space 2-point correlation functions.

Key words: cosmology: large-scale structure of Universe – galaxies: haloes – methods: statistical – methods: numerical

1 INTRODUCTION

Current and upcoming large-scale galaxy surveys will collect an extraordinary amount of data that encode rich information in both cosmology and galaxy physics. Spectroscopic surveys such as the Dark Energy Spectroscopic Instrument (DESI; [DESI Collaboration et al. 2016](#)), the Subaru Prime Focus Spectrograph (PFS; [Takada et al. 2014](#)), the ESA *Euclid* satellite mission ([Laureijs et al. 2011](#)) in addition to photometric surveys like the Rubin observatory-LSST ([Ivezić et al. 2019](#)) are expected to extend our current reach in both volume and depth by an order of magnitude. The volume and precision of the data require a robust modeling framework that can fully utilize the information content of the datasets and derive stringent and unbiased constraints on cosmology and galaxy physics.

One key requirement of such robust modeling framework is that it maximally captures the information contained in the clustering data down to small scales ($\approx 1 - 30\text{Mpc}/h$), which is coincidentally where modern surveys also have their highest signal-to-noise. Existing analyses of galaxy survey data almost exclusively utilize the galaxy 2-point correlation function (2PCF) as the summary statistics of the galaxy clustering. While the 2PCF is powerful in characterizing Gaussian density fields on large scales, it leaves out significant amount of information when applied to small scales, where the non-

linear evolution post shell-crossing and the complex physics of galaxy evolution become important. Therefore, the challenge of extracting the full information from small-scale clustering necessarily require the development and analysis of novel statistics beyond the 2PCF (e.g. [Paillas et al. 2023](#); [Valogiannis & Dvorkin 2022](#); [Banerjee & Abel 2021a](#); [Hahn et al. 2020](#); [Uhlemann et al. 2020](#); [Yuan et al. 2017](#); [Slepian et al. 2017](#)).

Another challenge in modeling small scales is that the standard perturbative models break down because of the complex non-linear evolution. Thus, considerable recent modeling efforts have been devoted to developing large N-body cosmological simulations, which can provide accurate model templates of the dark matter field down to arbitrarily small scales given sufficient computational resources (Recent examples include [Maksimova et al. 2021](#); [DeRose et al. 2019](#); [Ishiyama et al. 2021](#)). However, N-body simulations only simulate the gravitational growth of the total matter field, so we still need a robust so-called galaxy–dark matter connection model that “paints” galaxies on top of the simulated matter density field in order to generate forward models of the observed galaxy field (See [Wechsler & Tinker 2018](#) for a review). The extra information captured with beyond-2PCF statistics at small scales can be particularly powerful in constraining the galaxy–dark matter connection model, which would not only reveal details of galaxy evolution physics, but also feed back into the cosmology analysis and derive stronger cosmological constraints.

^{*} E-mail: sihany@stanford.edu

In this paper, we continue on previous work presented in [Banerjee & Abel \(2021a\)](#) and introduce observationally motivated generalizations of the k -th nearest neighbor (k NN) statistics. We demonstrate their constraining power on the galaxy–dark matter connection models through both theoretical arguments and a set of fully realistic mock tests. For the latter, we adopt the lightcone-based full forward model approach described in [Yuan et al. \(2023\)](#) to conduct parameter recovery tests while accounting for the full range of observational systematics, including redshift evolution and layers of survey incompleteness. We demonstrate that despite the observational systematics, our proposed 2D k NN variations yield unbiased yet significantly tighter constraints on galaxy–halo connection than the 2PCF.

The paper is organized as follows. In section 2, we describe the basic framework for our models and mock production. In section 3, we give an overview of the relevant summary statistics, the 2PCF, and the k -th nearest neighbor statistics with 2D generalizations. In section 4, we describe our fully realistic mock test and compare the model constraints of the 2PCF and the k NNs, including a discussion of galaxy assembly bias. In section 5, we provide additional discussion of our results and draw a few conclusions.

2 SIMULATION AND MOCKS

In this section, we introduce the simulation-based model template used in the ensuing analysis and the construction of our realistic lightcone-based mocks.

2.1 ABACUSUMMIT lightcones

The ABACUSUMMIT simulation suite ([Maksimova et al. 2021](#)) is a set of large, high-accuracy cosmological N-body simulations using the ABACUS N-body code ([Garrison et al. 2019, 2021](#)), designed to meet and exceed the Cosmological Simulation Requirements of the Dark Energy Spectroscopic Instrument (DESI) survey ([Levi et al. 2013](#)). ABACUSUMMIT consists of over 150 simulations, containing approximately 60 trillion particles at 97 different cosmologies. For this analysis, we use exclusively the “base” configuration boxes within the simulation suite, each of which contains 6912^3 particles within a $(2h^{-1}\text{Gpc})^3$ volume, corresponding to a particle mass of $2.1 \times 10^9 h^{-1} M_\odot$.¹ The ABACUSUMMIT suite also uses a specialized spherical-overdensity based halo finder known as COMPASO ([Hadzhiyska et al. 2022a](#)).

In addition to periodic boxes, the simulation suite also provides a set of simulation lightcones at fiducial cosmology ([Hadzhiyska et al. 2022b](#)). The basic algorithm associates the halos from a set of coarsely-spaced snapshots with their positions at the time of light-cone crossing by matching halo particles to on-the-fly light cone particles. The resulting halo catalogs are considered reliable at $M_{\text{halo}} > 2.1 \times 10^{11} h^{-1} M_\odot$. For this analysis, we utilize the 25 base lightcones, which are constructed from the 25 base periodic boxes, with each lightcone covering an octant of the sky ($\sim 5156 \text{ deg}^2$) up to $z \sim 0.8$.

A suite of lightcones at non-fiducial cosmologies are also being produced and will enable emulator cosmology analysis.

2.2 The Halo Occupation Distribution (HOD)

The galaxy–halo connection model we use for generating the realistic mocks and for the forward model is known as the Halo Occupation Distribution (HOD; e.g. [Zheng et al. 2005, 2007](#)), which probabilistically populate dark matter halos with galaxies according to a set of halo properties. For a Luminous Red Galaxy (LRG) sample, the HOD is well approximated by a vanilla model given by (originally shown in [Kwan et al. \(2015\)](#)):

$$\bar{n}_{\text{cent}}^{\text{LRG}}(M) = \frac{f_{\text{ic}}}{2} \text{erfc} \left[\frac{\log_{10}(M_{\text{cut}}/M)}{\sqrt{2}\sigma} \right], \quad (1)$$

$$\bar{n}_{\text{sat}}^{\text{LRG}}(M) = \left[\frac{M - \kappa M_{\text{cut}}}{M_1} \right]^\alpha \bar{n}_{\text{cent}}^{\text{LRG}}(M), \quad (2)$$

where the five vanilla parameters characterizing the model are M_{cut} , M_1 , σ , α , κ . M_{cut} characterizes the minimum halo mass to host a central galaxy. M_1 characterizes the typical halo mass that hosts one satellite galaxy. σ describes the steepness of the transition from 0 to 1 in the number of central galaxies. α is the power law index on the number of satellite galaxies. κM_{cut} gives the minimum halo mass to host a satellite galaxy. We have added a modulation term $\bar{n}_{\text{cent}}^{\text{LRG}}(M)$ to the satellite occupation function to remove satellites from halos without centrals. We have also included an incompleteness parameter f_{ic} , which is a downsampling factor controlling the overall number density of the mock galaxies. This parameter is relevant when trying to match the observed mean density of the galaxies in addition to clustering measurements. By definition, $0 < f_{\text{ic}} \leq 1$.

In addition to determining the number of galaxies per halo, the standard HOD model also dictates the position of velocity of the galaxies. For the central galaxy, its position and velocity are set to be the same as those the halo center, specifically the L2 subhalo center-of-mass for the COMPASO halos. For the satellite galaxies, they are randomly assigned to halo particles with uniform weights, each satellite inheriting the position and velocity of its host particle.

For this paper, we fix two parameters σ and κ for simplicity. κ does not strongly affect clustering and only comes into effect at very small scales. σ does affect clustering on 2-halo scales, but it tends to be strongly degenerate with $\log M_{\text{cut}}$. We omit σ in this preliminary analysis for clearer interpretation of the results.

We also include an additional HOD extension known as velocity bias, which biases the velocities of the central and satellite galaxies. This is shown to be a necessary ingredient in modeling BOSS LRG redshift-space clustering on small scales (e.g. [Guo et al. 2015; Yuan et al. 2021](#)). Velocity bias has also been identified in hydrodynamical simulations and measured to be consistent with observational constraints (e.g. [Yuan et al. 2022; Ye et al. 2017](#)).

We parametrize velocity bias through two additional HOD parameters: $\alpha_{\text{vel,c}}$ is the central velocity bias parameter, which modulates the peculiar velocity of the central galaxy relative to the halo center. $\alpha_{\text{vel,c}} = 0$ indicates no central velocity bias, i.e. centrals perfectly track the velocity of halo centers. $\alpha_{\text{vel,s}}$ is the satellite velocity bias parameter, which modulates how the satellite galaxy peculiar velocity deviates from that of the local dark matter particle. $\alpha_{\text{vel,s}} = 1$ indicates no satellite velocity bias, i.e. satellites perfectly track the velocity of their underlying particles.

For computational efficiency, we adopt the highly optimized ABACUSHOD implementation, which significantly speeds up the HOD calculation per HOD parameter combination ([Yuan et al. 2021](#)). The code is publicly available as a part of the ABACUSUTILS package at <https://github.com/abacusorg/abacusutils>. Example usage can be found at <https://abacusutils.readthedocs.io/en/latest/hod.html>.

¹ For more details, see <https://abacussummit.readthedocs.io/en/latest/abacussummit.html>

To summarize, for this analysis, the HOD is fully parameterized by 6 parameters, M_{cut} , M_1 , α , $\alpha_{\text{vel},c}$, $\alpha_{\text{vel},s}$, and f_{ic} . Additionally, in section 4.4, we further extend this HOD model with galaxy assembly bias.

2.3 Realistic mocks

We construct our realistic mocks on 20 base lightcones **ph005-024** at Planck cosmology. To generate galaxies on these lightcones, we start by picking an HOD that roughly matches the properties of the BOSS CMASS sample. The parameters are $\log M_{\text{cut}} = 12.8$, $\log M_1 = 13.9$, $\sigma = 0.3$, $\alpha = 1.0$, $\kappa = 0.3$, velocity bias parameters $\alpha_{\text{vel},c} = 0.2$, $\alpha_{\text{vel},s} = 1$, and an completeness parameter $f_{\text{ic}} = 0.41$ (Yuan et al. 2021). We then follow the procedures laid out in Yuan et al. (2023) to apply layers of survey realism on to the lightcone mocks, including redshift-based incompleteness, survey geometry and various survey masks. We ignore fiber collision for this analysis. However, we do emphasize that we have devised a generic method of correcting for the effect of fiber collision on any summary statistics via probabilistic redshift recoveries, as laid out in section 3 of Yuan et al. (2023).

3 SUMMARY STATISTICS FOR GALAXY CLUSTERING

Commonly, we compare the model to the data through a set of compression known as summary statistics. The use of summary statistics drastically reduces the degrees of freedom in the likelihood function and also marginalizes over stochastic components in the data that are hard to model. However, the downside of summary statistics is that they are lossy compressions and do not typically capture the full information of the density field. Thus, it is important to develop summary statistics that maximize both the simplicity of analysis and the information content, especially considering the high cost and tremendous data volumes of modern large-scale structure experiments.

In this section, we first revisit the standard 2-point correlation function before introducing the k -th nearest neighbor statistics (kNN) and its 2D generalizations. All visualizations of the summary statistics and their covariance matrices are measured from the mock galaxy catalogs described in the previous section.

3.1 2-point correlation function

The most widely used summary statistics in large-scale structure studies is the 2-point correlation function (2PCF) and its Fourier space counterpart, the power spectrum. In principle, the 2PCF fully summarizes the information content of the Gaussian random field, which is a valid approximation on very large scales but quickly breaks down on smaller scales. Mathematically, the real space two-point correlation function $\xi(r)$ describes the excess probability above Poisson samples for a galaxy to be located in subvolume dV_1 at distance r from another galaxy in subvolume dV_2 .

$$dP_{12} = \bar{n}^2 [1 + \xi(r)] dV_1 dV_2, \quad (3)$$

where \bar{n} is the average number density of galaxies over the volume considered (Peebles 1980).

In redshift space, the Line-of-sight (LoS) positions of galaxies are distorted by their peculiar velocities. This effect is known as redshift-space distortions. However, we can still exploit rotation symmetry around the LoS axis and consider the full shape 2PCF in redshift space as a 2D function $\xi(r_p, r_\pi)$. r_p and r_π are the transverse and

LoS separations in comoving units. In practice, $\xi(r_p, r_\pi)$ can be computed via the unbiased Landy & Szalay (1993) estimator:

$$\xi(r_p, r_\pi) = \frac{DD - 2DR + RR}{RR}, \quad (4)$$

where DD , DR , and RR are the normalized numbers of data-data, data-random, and random-random pair counts in each bin of (r_p, r_π) . The transverse vs LoS decomposition is particularly convenient as it forms the natural basis that different physical phenomena and systematics operate in. Most significantly, redshift-space distortion, which is the clustering modulation due to velocity dispersion along the LoS only affects clustering along r_π . While the systematic effects such as fiber collision and survey geometry only affects the observed clustering along the transverse r_p direction.

While the 2PCF fully captures the information in a Gaussian field, it fails to capture non-gaussian information sourced in variations in primordial inflationary fluctuations and the late time gravitational evolution (e.g. Carron 2012; Takada & Jain 2003). On the observational front, the 2PCF is also challenging because it is sensitive to a range of observational systematics, particularly incompleteness due to fiber collision and survey geometry, whose effects propagate through all scales of the 2PCF.

The 2PCF is also relatively expensive to compute, as the pair finding step in principle scales as the square of the number of points. However, highly-optimized grid-based method to compute the 2PCF have been developed, such as CORRFUNC (Sinha & Garrison 2020), which employs various algorithmic optimizations and hardware acceleration for faster calculations.

For this paper, we use the full-shape redshift-space 2PCF $\xi(r_p, r_\pi)$ for comparison with other statistics and choose the following binning: 14 logarithmic bins in r_p between $0.5h^{-1}\text{Mpc}$ and $30h^{-1}\text{Mpc}$ and 10 linear bins in r_π between 0 and $30h^{-1}\text{Mpc}$, for a total of 140 bins. We choose the minimum r_p to be $0.5h^{-1}\text{Mpc}$ as smaller scales are strongly affected by fiber collision, given the fiber collision recovery scheme that we described in the Yuan et al. (2023). We calculate $\xi(r_p, r_\pi)$ in such configuration on a HOD-based galaxy mock resembling CMASS and visualize the result in Figure 1. We showcase the corresponding covariance matrix in Figure 2, where the axes represent the bins flattened by column, with r_p increasingly monotonically in bin number.

3.2 1D kNN s

The limits of the 2PCF on small scales necessitates the development of additional summary statistics. One such statistic is the k -th nearest neighbor statistics, or kNN s for short (Banerjee & Abel 2021a,b; Wang et al. 2022). The kNN s are conceptually straightforward – measuring the distances to the k -th nearest neighbor galaxy in a dataset measured from a set of volume-filling query points, and computing the cumulative distribution of these distances. Banerjee & Abel (2021a,b) showed through Fisher forecasts that kNN s are highly informative on cosmology and are sensitive to all orders of n -point correlation functions. We offer a brief review in this sub-section.

To construct the 1D kNN s, we start with a set of N_D data points in total volume V_{tot} . We place a set of N_R random points over the entire volume. Given these random points, we compute the distance from each of these random points to the k -th nearest neighbor in the original dataset for a given value of k . This can be done very efficiently with the construction of a KD -Tree on the data points. We then compute the empirical CDF of distances to the k -th nearest neighbor as $\text{CDF}_{kNN}(r)$, i.e. the fraction of random points with distance to the k -th nearest neighbor $< r$. This CDF is precisely also

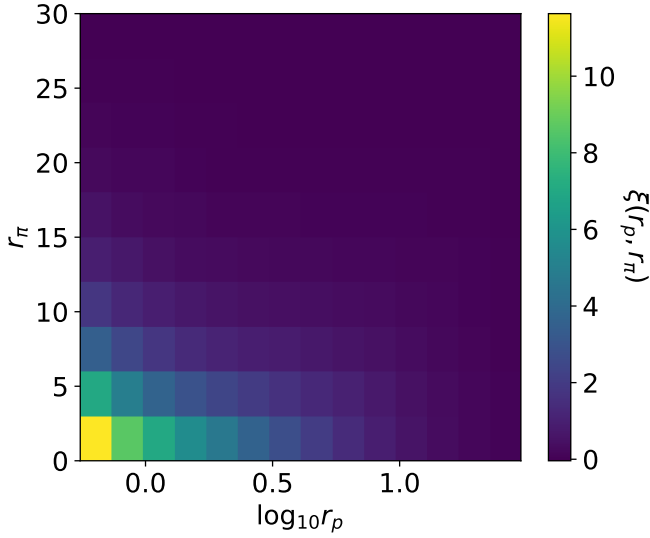


Figure 1. The target mock 2PCF $\xi(r_p, r_\pi)$ calculated on the 20 lightcone mocks. We choose the minimum r_p to be $0.5h^{-1}\text{Mpc}$ as smaller scales are strongly affected by fiber collision, given the fiber collision recovery scheme that we described in the [Yuan et al. \(2023\)](#).

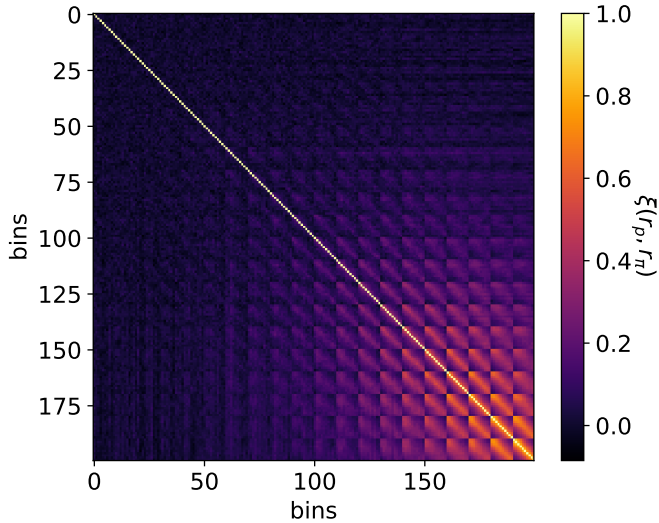


Figure 2. The mock correlation matrix of the two-dimensional 2PCF $\xi(r_p, r_\pi)$. The x and y axes denote the bins collapsed to 1D, by concatenating the columns shown in Figure 1. The covariance matrix is calculated by applying a fiducial HOD to the 1800 ABACUSUMMIT covariance boxes, each of volume $(500h^{-1}\text{Mpc})^3$. We refer the readers to section 4 of [Yuan et al. \(2023\)](#) for details.

the fraction of randomly placed spheres enclosing $> k - 1$ points at a given r . We can write this down as

$$\text{CDF}_{k\text{NN}}(r) = P_{>k-1|V} \big|_{V=\frac{4\pi}{3}r^3}. \quad (5)$$

Because of the nature of CDFs, for large scales very significant changes in the $k\text{NN}$ -CDF can be of very small magnitude as the statistic asymptotes to 1. Therefore, for visualization purposes it is

sometimes beneficial to plot the peaked CDF (PCDF), defined as:

$$\text{PCDF}(r) = \begin{cases} \text{CDF}(r) & \text{CDF}(r) \leq 0.5 \\ 1 - \text{CDF}(r) & \text{CDF}(r) > 0.5 \end{cases}. \quad (6)$$

We refer the reader to [Banerjee & Abel \(2021a\)](#) for example illustrations of the peaked CDF. The visualizations in this paper are shown in the CDF form.

For physical intuition, the $k\text{NN}$ -CDFs are directly related to counts-in-cell statistics. Specifically, from Equation 5, we can write down the counts-in-cell distribution as the difference between two $k\text{NN}$ s. Specifically, starting from a random point, the probability of finding exactly k neighbors at radius r is

$$P_{k|V} = \text{CDF}_{k\text{NN}}(r) - \text{CDF}_{(k+1)\text{NN}}(r). \quad (7)$$

This shows that the counts-in-cells and $k\text{NN}$ s at a given radius are equivalent descriptions of the underlying data, and that one can easily be computed once the other is known. Additionally, $P_{0|V}$ is also known as the void probability function, which characterizes the distribution of voids as a function of void size ([White 1979](#)). The fact that both counts-in-cell statistics and void probability functions can be straightforwardly derived from $k\text{NN}$ s is a strongly indicative of its rich information content.

3.3 2D $k\text{NN}$ s

While we have just described $k\text{NN}$ s as 1D functions of radial separation r , one can also decouple the distance dependency into a LoS component r_π and a transverse component r_p , analogous to the scale decomposition we introduced for the 2PCF. We speculate that we could gain significantly more information compared to the 1D $k\text{NN}(r)$ by disentangling the effects of the redshift-space distortion signatures on the small scales. This point was showcased for the 2PCF in [Yuan et al. \(2021\)](#).

Thus, we introduce the 2D $k\text{NN}$ -CDF in the (r_p, r_π) basis. Specifically, we decompose the distance between each query-data pair r into a r_p and a r_π component, and we bin both projections into a 2D histogram. Then we calculate a 2D CDF where each bin accumulates the counts from all bins with smaller r_p and r_π . Finally, we normalize the cumulative counts by the total number of query points. Conceptually, the 2D $k\text{NN}$ -CDF is exactly analogous to the default 1D $k\text{NN}$ -CDF, except we tabulate distances and the cumulative statistics in 2D. For the rest this paper, we denote the default 1D $k\text{NN}$ -CDF as “ $k\text{NN}(r)$ ” and the new 2D $k\text{NN}$ -CDF as “ $k\text{NN}(r_p, r_\pi)$ ”.

For intuition, we plot the first four orders of $k\text{NN}(r_p, r_\pi)$ in Figure 3. In each panel, the 2D heatmap and the solid contours showcase the 2D $k\text{NN}$ CDF of a mock galaxy sample resembling CMASS. By definition, the CDF monotonically increases from 0 at very small separation to 1 at very large separation. In each panel, the solid contours correspond to CDF values of 0.05, 0.15, 0.25,..., 0.95. The dotted contours showcase the corresponding CDF of an un-clustered Poisson random sample of the same size. The difference between the solid and dotted lines showcase the signatures of clustering. As expected, for larger CDF values, the solid contours reach the same CDF values at larger radii. This is because the query points uniformly sample the entire volume, and thus predominantly occupy voids. As a result, the distance between queries and galaxies can be thought of as a measure of void sizes. Qualitatively, the more clustered the galaxies are, the larger the voids tend to be, and thus the larger distances between queries and their k -th nearest galaxy neighbors.

For this analysis, we set up our $k\text{NN}(r_p, r_\pi)$ data vector as the following: we use 8 logarithmic bins along the r_p direction between $0.32h^{-1}\text{Mpc}$ and $63h^{-1}\text{Mpc}$, and 5 logarithmic bins along

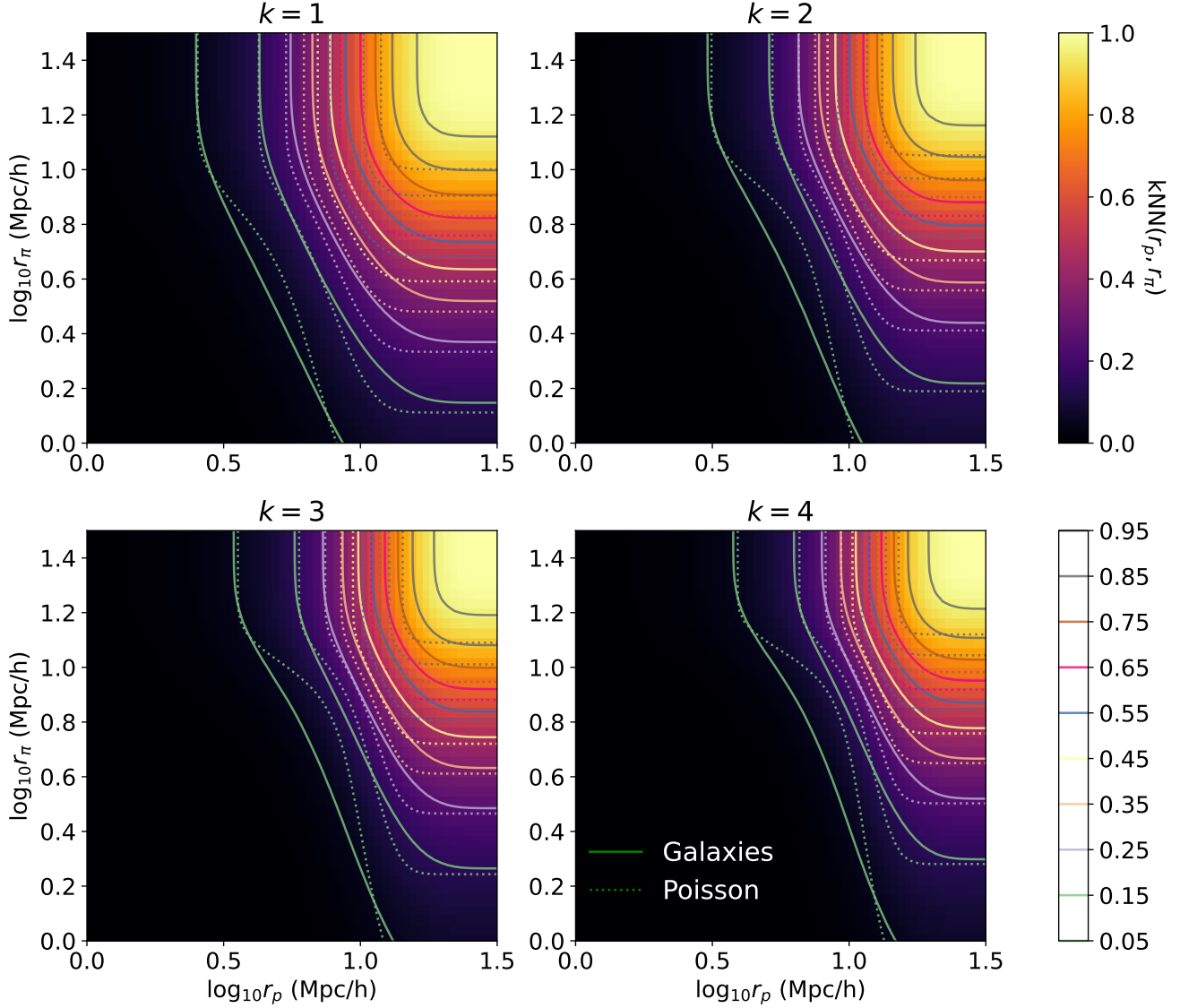


Figure 3. Visualizations of the 2D $kNN(r_p, r_\pi)$ as a function of transverse separation r_p and line-of-sight separation r_π . The 2D heatmap showcases the 2D CDF for $k = 1, 2, 3, 4$. The solid contours highlight the features of the CDF. The dashed contours show the same CDF values for a Poisson random field of the same number of galaxies. The difference in the solid and dashed lines showcase the regions containing the clustering information.

the r_π direction between $1h^{-1}\text{Mpc}$ and $32h^{-1}\text{Mpc}$. We start with $k = 1, 2, 3, \dots, 10$ similar to the 1D case. The corresponding covariance matrix is shown in Figure 5. The covariance matrix is calculated by applying a fiducial HOD to the 1800 ABACUSSUMMIT covariance boxes, each of volume $(500h^{-1}\text{Mpc})^3$. We refer the readers to section 4 of Yuan et al. (2023) for details. The relatively coarse sampling of scale along r_p and r_π is chosen to control the size of the data vector to be much less than the number of independent mocks available for covariance matrix calculation. We use the same bin flattening scheme as for $\xi(r_p, r_\pi)$.

3.4 2D Data-data kNN s

We introduce an additional flavor of 2D kNN in what we call the data-data kNN , or DD- kNN . In the standard kNN formalism, the distances are measured between data points and query points. However, one

can also measure such distances between data points and other data points, analogous to the DD pair counts in correlation statistics. For this reason, the DD- kNN is closely related to the 2-point correlation functions and contains a different set of information than the standard kNN statistics. Specifically, in the standard kNN , the query points are drawn randomly and thus mostly sample the under-dense regions of the density field, but in DD- kNN , the query points are the same as data points, thus the DD- kNN tracks the over-dense regions, similar to the 2-point correlation function. Because of this, we speculate that the DD- kNN is likely more sensitive to small-scale effects and 1-halo scale physics. Another way to think about the difference between the standard kNN and the DD- kNN is that the standard kNN tracers the density field, and is qualitatively a 1-point statistics, whereas the DD- kNN traces the clustering, and is thus more akin to a 2-point clustering statistics. In fact, we show in the next paragraphs that the DD- kNN exactly derives the 2-point correlation function. In this

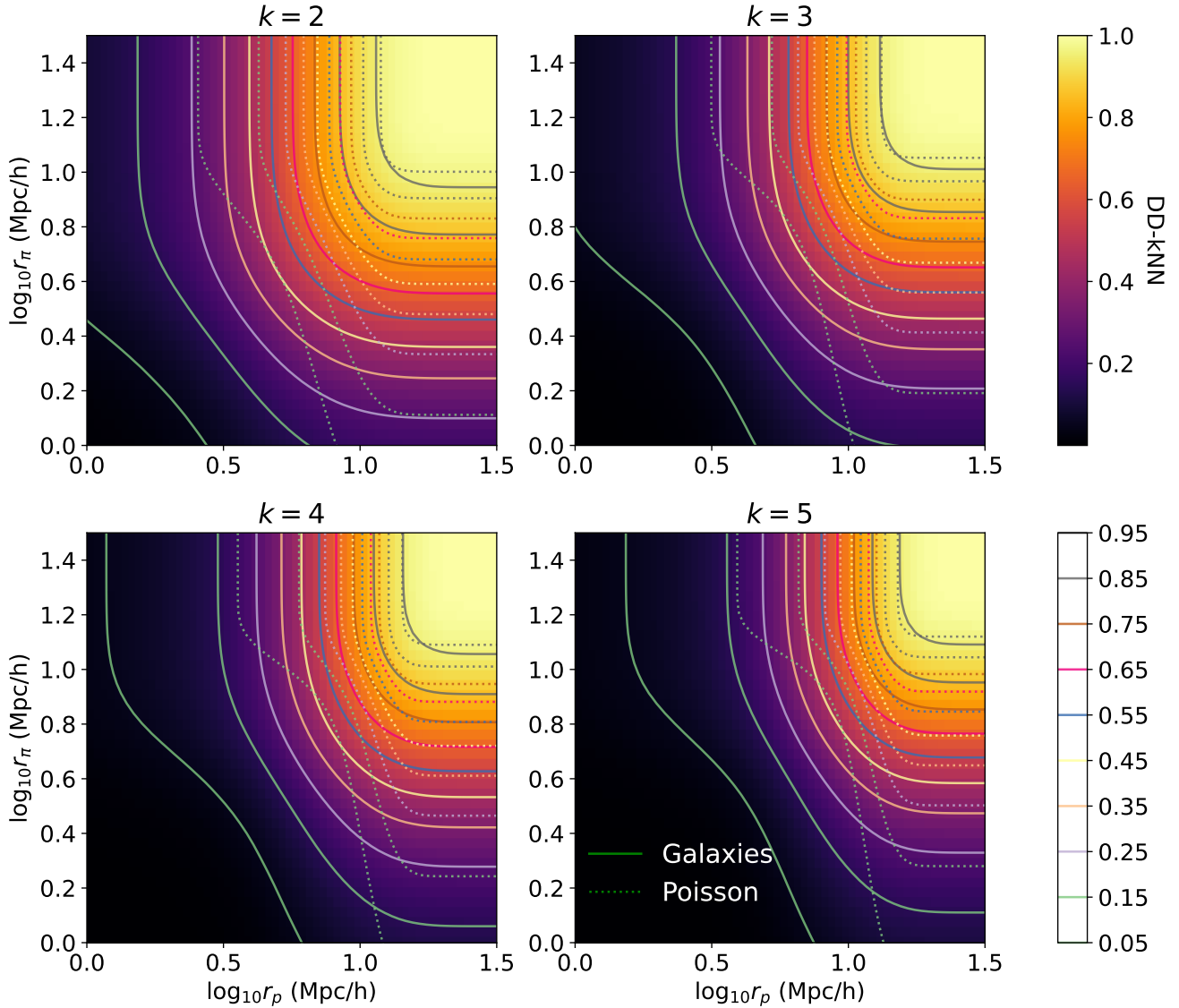


Figure 4. Visualizations of the DD- k NN as a function of transverse separation r_p and line-of-sight separation r_π . The 2D heatmap showcases the 2D CDF for $k = 2, 3, 4, 5$. The solid contours highlight the features of the CDF. The dashed contours show the same CDF values for a Poisson random field of the same number of galaxies. The difference in the solid and dashed lines showcase the regions containing the clustering information.

paper, we use “DD- k NN” to specifically refer to the 2D k NN(r_p, r_π) but with data-data pairs instead of query-data pairs.

Figure 4 visualizes the DD- k NN for $k = 2, 3, 4, 5$. Note that in our definition each galaxy’s nearest galaxy neighbor is itself, so DD-1NN = 1. Compared to the standard k NN(r_p, r_π), the DD- k NN CDF reaches the same values at a much smaller separation, consistent with the notion that DD- k NN traces high density regions. The contours for an un-clustered Poisson sample also show more dramatic departures from the galaxy contours, suggesting that the DD- k NN is highly sensitive to clustering.

Now we demonstrate that the 2PCF directly derives from the DD- k NN. We can think of the 2PCF as the mean overdensity of galaxies around other galaxies, and one can derive this mean overdensity by also integrating over the the PDF derivatives of the DD- k NN over all k s. Mathematically, we can first write down the 2D PDFs similar

to Equation 5

$$P_{k|\leq r_p, \leq r_\pi} = \text{CDF}_{k\text{NN}}(r_p, r_\pi) - \text{CDF}_{(k+1)\text{NN}}(r_p, r_\pi). \quad (8)$$

$P_{k|\leq r_p, \leq r_\pi}$ gives the probability of finding exactly k galaxies at or within the cylinder defined by radius r_p and height $2r_\pi$ around a given galaxy. Then we can differentiate $P_{k|\leq r_p, \leq r_\pi}$ against both r_p and r_π to get the probability of finding the k -th galaxy neighbor at (r_p, r_π) separation away from a given galaxy,

$$P_{k|r_p, r_\pi} = \frac{\partial^2 P_{k|\leq r_p, \leq r_\pi}}{\partial r_p \partial r_\pi}. \quad (9)$$

Finally, we can now express the 2PCF, or the mean overdensity profile of galaxies around a given galaxy as,

$$\xi(r_p, r_\pi) = \frac{\sum_{k=1}^{\infty} k P_{k|r_p, r_\pi}}{DR} - 1. \quad (10)$$

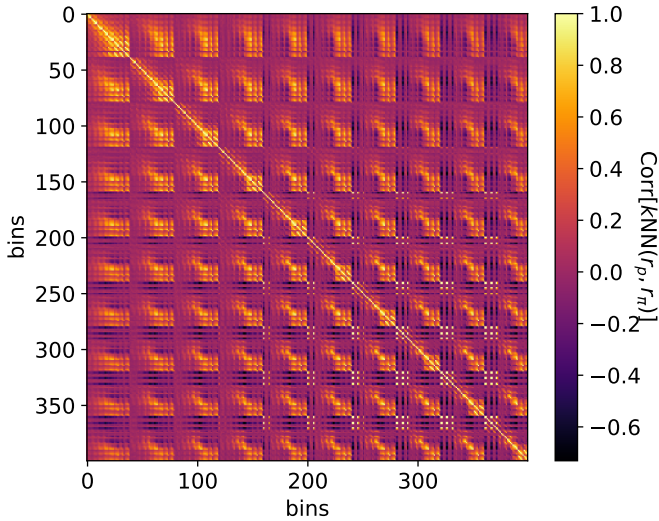


Figure 5. The mock correlation matrix of the two-dimensional $kNN(r_p, r_\pi)$ for $k = 1, 2, 3, \dots, 10$. The x and y axes denote the bins collapsed to 1D, with r_p increasingly monotonically in bin number. The covariance matrix is calculated by applying a fiducial HOD to the 1800 ABACUSUMMIT covariance boxes, each of volume $(500h^{-1}\text{Mpc})^3$. We refer the readers to section 4 of Yuan et al. (2023) for details.

Here we have simply written the denominator as DR , which denotes the expected number of galaxies expected at the same separation if the galaxy field is unclustered. One can analytically compute DR as mean density multiplied by the volume of the (r_p, r_π) voxel. We also point out that while we have adopted the (r_p, r_π) basis for this derivation, this connection between DD- kNN to 2PCF is generic to any scale basis.

For this analysis, we set up the DD- $kNN(r_p, r_\pi)$ data vector as follows: we use 8 logarithmic bins along the r_p direction between $0.63h^{-1}\text{Mpc}$ and $63h^{-1}\text{Mpc}$, and 5 logarithmic bins along the r_π direction between $0.5h^{-1}\text{Mpc}$ and $32h^{-1}\text{Mpc}$. We include k orders $k = 2, 3, \dots, 10$. Compared to the regular $kNN(r_p, r_\pi)$, we extend the DD- kNN down to smaller scales because we expect it to better capture the high density regions and thus show signal down to smaller scales. The corresponding covariance matrix is shown in Figure 6.

Finally, we highlight that despite that the standard query-data kNN and the data-data kNN are phrased and computed in similar ways, the two statistics are likely sensitive to different scales and trace different moments of the over-density field. We expect the two statistics to be highly complimentary and result in different model degeneracies. We demonstrate this point in the following section.

3.5 Computational cost

One of the key advantages of kNN and other density-style statistics over higher-order correlation functions is low computational cost. While the cost of n -point correlation functions in principle scales with N^n , where N is the number of galaxies in the sample, kNN s only scales as $N \log N$. In our analysis, we indeed find the kNN calculation to be comparable to a highly optimized $N \log N$ 2PCF calculator (CORRFUNC (Sinha & Garrison 2020)).

To further accelerate calculation of kNN in both 1D and 2D, we created a publicly available kNN library `FNNTW` which achieves high

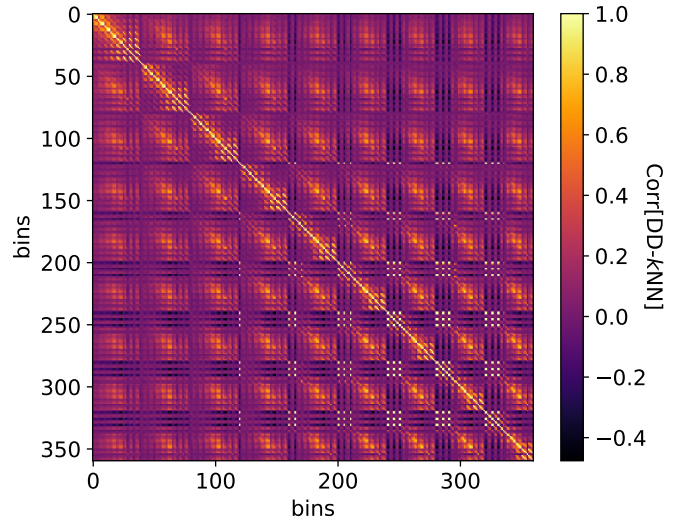


Figure 6. The mock correlation matrix of the two-dimensional DD- $kNN(r_p, r_\pi)$ for $k = 2, 3, \dots, 10$. The x and y axes denote the bins collapsed to 1D, with r_p increasingly monotonically in bin number.

performance by offering parallel builds and a specialized query for the 2D kNN . The code is written in RUST² and bindings are made available for PYTHON³. Parallelism is achieved in the builds through two avenues not present in other PYTHON kD -Tree libraries. Firstly, we note that every subtree of a kD -Tree is an independent kD -Tree which can be built on a separate thread. The library offers a build method which parallelizes the builds for a subset of these subtrees. Secondly, on a serial build that uses a selection algorithm to find the median and partition the space, we find that approximately 95% of the run time is spent on the selection algorithm. As such, while the subtree size is above an empirically determined threshold we use a parallel median-of-medians algorithm to find an approximate median with which to partition the space. This shortens the build time of large trees without degrading query performance. For 2D queries, `FNNTW` provides a custom query method which returns the line-of-sight and parallel components, adding a negligible cost over a query that only returns the Euclidean distance. We refer the readers to the linked website for performance benchmarks against other popular kD -Tree codes.

For a reference performance benchmark for cosmology, we populate a $2000h^{-1}\text{Mpc}$ cubic box with 4 million galaxies with a CMASS-like HOD and also 1 million random query points. The workstation used for this test has dual Intel Xeon Gold 5218 chips clocked at 2.3 GHz for a total of 32 physical cores and 256 GB DDR4-2666 RAM. Using 32 threads, the 2PCF $\xi(r_p, \pi)$ calculation with CORRFUNC took 0.44 seconds. In comparison, the DD- kNN calculation including $k = 2, 3, \dots, 10$ took 1.4 seconds. The standard $kNN(r_p, r_\pi)$ calculation for $k = 1, 2, \dots, 9$ took 1.7 seconds. While the 2PCF code is faster in this specific setup, we note that CORRFUNC is grid-based and thus scales very well at large sample sizes. If we decrease the sample size to 200,000, the tree-based DD- kNN compute time drops to 0.11 seconds, whereas the $\xi(r_p, \pi)$ times drops only to 0.15 seconds. This suggests that when confronted with large data volumes

² <https://crates.io/crates/fnntw/>

³ <https://pypi.org/project/pyfnntw/>

with upcoming surveys, it is likely beneficial to develop a grid-based k NN code.

Nevertheless, it is impressive that our computational performance with k NN is already comparable to the highly developed 2PCF codes. More importantly, k NN calculation scales cheaply in k . For example, going from the first 10 k s to the first 20 k s only increase the compute time by 50%. Thus, k NNs represent a very cheap way of incorporating high-order clustering information, especially when compared to directly computing n -point correlation functions.

4 HOD RECOVERY ON REALISTIC LIGHTCONE MOCKS

In this section, we test and compare the constraining power of the summary statistics described in section 3 by recovering the underlying HOD parameters on a realistic galaxy mock. We first describe the construction of the lightcone mock, then we describe the modeling pipeline before we present the recovered HOD posterior.

4.1 Mock data setup

We first set up the mock target data vectors using the realistic lightcone-based mocks described in section 2. The set up is also identical to that of Yuan et al. (2023), where we describe the layers of realism applied to the mock in great detail.

For the 2PCF, we use the full 2D decomposition $\xi(r_p, r_\pi)$ as our summary statistic. Specifically, we choose 14 logarithmic bins between $0.5h^{-1}\text{Mpc}$ and $30h^{-1}\text{Mpc}$ along the transverse direction, and 10 linear bins between 0 and $30h^{-1}\text{Mpc}$ along the LOS direction, for a total of 140 bins. We visualize the mock target $\xi(r_p, r_\pi)$ in Figure 1.

For the 1D k NN(r), we use the first 10 orders, $k = 1, 2, 3, \dots, 10$. For each k , we sample the CDF at 50 linearly spaced scales between $r_{\min} = 0.1h^{-1}\text{Mpc}$ and $r_{\max} = 20h^{-1}\text{Mpc}$. We further remove scales where the CDF is less than 0.1 or greater than 0.9 as these points tend to highly covariant and lead to very poorly behaved covariance matrices. As a result, we end up with 219 points across 10 k s. We refer the readers to Figure 5 and Figure 7 of Yuan et al. (2023) for visualizations of k NN(r).

For the k NN(r_p, r_π), we use 8 logarithmic bins along the r_p direction between $0.63h^{-1}\text{Mpc}$ and $63h^{-1}\text{Mpc}$, and 5 logarithmic bins along the r_π direction between $1h^{-1}\text{Mpc}$ and $32h^{-1}\text{Mpc}$. We start with $k = 1, 2, 3, \dots, 10$ similar to the 1D case. Then, similar to the 1D case, we also remove bins where the CDF is less than 0.05 or greater than 0.95, where the variation is noise-dominated. 156 bins remain across the 10 k s. We adopt the same scheme for the DD- k NN except we skip $k = 1$.

4.2 Analysis pipeline

To recover the underlying HOD parameters from the summary statistics computed on the target mocks, we utilize the 5 remaining lightcones, phase ph000-004. For each model evaluation, we propose a set of HOD parameters from a flat prior, populate the 5 lightcones (ph000-004) with the proposed HOD, and then apply the systematics effects, including redshift selection, survey window and masks. Finally, we compute the summary statistics averaged over the 5 lightcones, which we compare with the target summary statistics and calculate likelihoods using the aforementioned covariance matrix. For this analysis, we adopt a Gaussian likelihood function that accounts for both the desired summary statistics and also the average

density. Specifically,

$$\log L = -\frac{1}{2}(x_{\text{proposed}} - x_{\text{target}})^T \mathbf{C}^{-1}(x_{\text{proposed}} - x_{\text{target}}) - \frac{1}{2} \frac{(\bar{n} - \bar{n}_{\text{target}})^2}{\sigma_n^2} \quad (11)$$

where x is the desired summary statistic, \mathbf{C} is the covariance matrix, and \bar{n} is the mean number density. σ_n is the uncertainty on the measured mean number density. For a CMASS-like sample, we quote $\sigma_n = 5\%$.

We sample the parameter posteriors with the DYNESTY nested sampler (Speagle & Barbary 2018; Speagle 2020). We impose flat priors bounded with an ellipsoid for all parameters. The ellipsoid is constructed as the minimum-volume ellipsoid that envelopes all training points. We initiate each nested sampling chain with 2000 live points and a stopping criterion of $d \log \mathcal{Z} = 0.01$, where \mathcal{Z} is the evidence. As expected, we achieve excellent fits for both summary statistics, with best-fit $\chi^2/\text{d.o.f} < 1$.

To accelerate the sampling, we substitute the likelihood evaluation with a fast emulator model. Specifically, we stop the explicit likelihood evaluation after 40,000 likelihood calls and use the samples to train a neural network model, which we then replace the explicit likelihood evaluations with in order to continue sampling. We validate and test our trained model to ensure that the predictions are unbiased and the errors are insignificant compared to other systematic errors. For all three statistics, we arrive at 30% emulation error compared to the expected sample variance, or 10% increase in amplitude to the covariance matrix. While insignificant, we include this additional error in our analysis. For details of this procedure, we refer the readers to section 4 of the companion paper Yuan et al. (2023).

Figure 7 visualizes the best-fit DD- k NN(r_p, r_π) statistic compared to the true mock data vector. Specifically, the y-axis shows the relative difference between the best-fit and the mock data normalized by the expected error bars. The panels show different k s while the colors represent different r_π bins. We see that the best fit is within 1σ of the data vector across all bins. The σ refers to the expected error bar normalized to the CMASS volume. We omit showing the best-fits of the other data vectors for brevity.

4.3 Parameter recovery

Figure 8 showcases the parameter posteriors for the 3 different configurations of the k NN statistics. Green represents the standard 1D k NN(r) statistic; red represents the 2D k NN(r_p, r_π) statistic; blue represents the DD- k NN statistic. The black lines show the underlying truth values. The marginalized constraints shown at the top of the 1D PDF plots are the posterior mean and 2σ constraints of the DD- k NN statistic. We also summarize the marginalized constraints in Table 1.

To quantify the difference in constraining power of the different summary statistics, we construct a Figure of Merit (FoM) metric as the following

$$\text{FoM} = [\text{Vol}(< 3\sigma)]^{-\frac{1}{n}}, \quad (12)$$

where n is the number of parameter in the model. $\text{Vol}(< 3\sigma)$ is the volume in the model parameter space of all samples within 3σ of the best-fit. We approximate this volume by computing the volume of the minimum enveloping ellipsoid of the 3σ samples. In this empirical scheme, the FoM roughly indicates the inverse of the constraint per parameter direction. The more informative statistics will have larger FoMs. We summarize the FoM values for the four summaries statistics in the bottom row of Table 1.

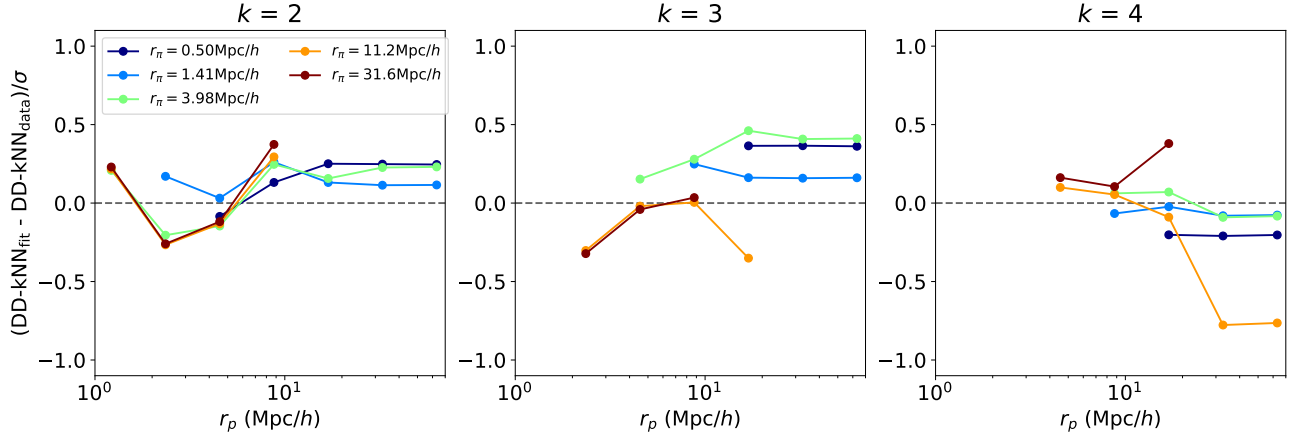


Figure 7. The best-fit DD- k NN(r_p, r_π) statistic compared to the truth. The y-axis shows the difference between the best fit and the mock data vector, normalized by CMASS error bar. The three panels refer to $k = 2, 3, 4$, respectively. Each color refers to a r_π bin. The segmentation is due to the bin cuts we placed to remove the tails of the CDF. We see that that we achieve a very good fit.

Parameter	truth	1D k NN(r) (95% C.L.)	k NN(r_p, r_π) (95% C.L.)	DD- k NN(r_p, r_π) (95% C.L.)	$\xi(r_p, r_\pi)$ (95% C.L.)
$\log_{10} M_{\text{cut}}$	12.8	12.800 ± 0.024	12.796 ± 0.019	12.797 ± 0.013	12.79 ± 0.02
$\log_{10} M_1$	13.9	12.93 ± 0.12	13.88 ± 0.06	13.89 ± 0.03	13.89 ± 0.07
α	1.0	1.00 ± 0.25	1.00 ± 0.12	0.99 ± 0.05	1.03 ± 0.16
$\alpha_{\text{vel},c}$	0.2	0.21 ± 0.18	0.19 ± 0.06	0.200 ± 0.014	0.20 ± 0.03
$\alpha_{\text{vel},s}$	1.0	0.93 ± 0.36	0.99 ± 0.14	1.00 ± 0.04	0.96 ± 0.08
FoM		4.2	11.4	32.0	15.5

Table 1. The posterior constraints of the 6 HOD model parameters recovered from the 2PCF w_p and variations of the k NNs. The bottom row indicates the Figure of Merit (FoM) of the four summary statistics (see Equation 12).

First of all, we get unbiased constraints on all parameters with each of the 3 k NN flavors. This adds support to the conclusions of our companion paper [Yuan et al. \(2023\)](#) and further confirms the efficacy of the lightcone-based full forward model approach for an additional set of statistics. We expect our forward model approach to also apply to other novel summary statistics.

Figure 8 also shows that, against the same mock galaxy catalog, and using the same k s and roughly the same scale cuts, the different formulations of the k NN statistics get drastically different constraints. Specifically, the k NN(r_p, r_π) is able to derive much stronger constraints than the standard 1D k NN. Furthermore, the 2D k NN with data-data pairs is able to further tighten the constraints on the HOD parameters. It is likely that the 2D formulations get stronger constraints because they disentangle the redshift-space distortion effects whereas the standard k NN(r) does not. Specifically, the line-of-sight structure on the small scales is strongly attributed to the velocity dispersion of the galaxies, which strongly depends on the 1-halo structure and the satellite fraction of the halos. Thus, capturing the RSD increases the constraining power on the HOD parameters. A similar effect was found for the 2PCF, where the full 2D $\xi(r_p, r_\pi)$ statistic was found to be significantly more constraining on HOD and assembly bias parameters than the projected 2PCF ([Yuan et al. 2021](#)).

The fact that the DD- k NN derives stronger constraints on the HOD than the standard k NN(r_p, r_π) is not surprising. The standard k NN tabulates distances to galaxy neighbors around randomly chosen query points. By definition, the query points will more likely populate low density regions instead of high density regions. Thus,

the standard k NN up-weights low density regions instead of high density regions. However, most of the HOD constraints come from high density regions, as luminous galaxies tend to live in the more massive halos, and satellite occupation is better constrained in the more massive halos. In the DD- k NN case, the query points are the galaxy positions, which populate dense regions more than underdense regions. Thus, the DD- k NN is expected to be much more sensitive to the HOD, thus yielding stronger constraints. Another way to understand the difference is that the DD- k NN is a mass-weighted re-average of the standard k NN, thus more sensitive to denser environments.

However, the three different flavors of k NNs do result in comparable constraining power on parameter $\log M_{\text{cut}}$ parameter. This parameter controls the central occupation in this model, and thus largely determines the amplitude of the galaxy power spectrum assuming a low satellite fraction. This suggests that all three flavors of k NNs can effectively capture the clustering amplitude. This in turn implies that the k NNs are potentially powerful probes for constraining cosmic growth rate, assuming we can disentangle galaxy bias from the underlying matter clustering amplitude. This is consistent with Fisher forecast results in [Banerjee et al. \(2022\)](#).

Figure 9 compares the parameter constraints from the 2D k NNs to the redshift-space 2PCF $\xi(r_p, r_\pi)$. The standard k NN(r_p, r_π) delivers roughly equivalent constraining power on the HOD compared to the 2PCF. However, the DD- k NN derives considerably stronger constraints than the 2PCF across all parameters, especially on the mass parameters $\log M_{\text{cut}}$ and $\log M_1$. This is consistent with the fact that the full shape 2PCF can be exactly derived from the DD- k NNs. The fact that the k NN constraints and the 2PCF have different degeneracy

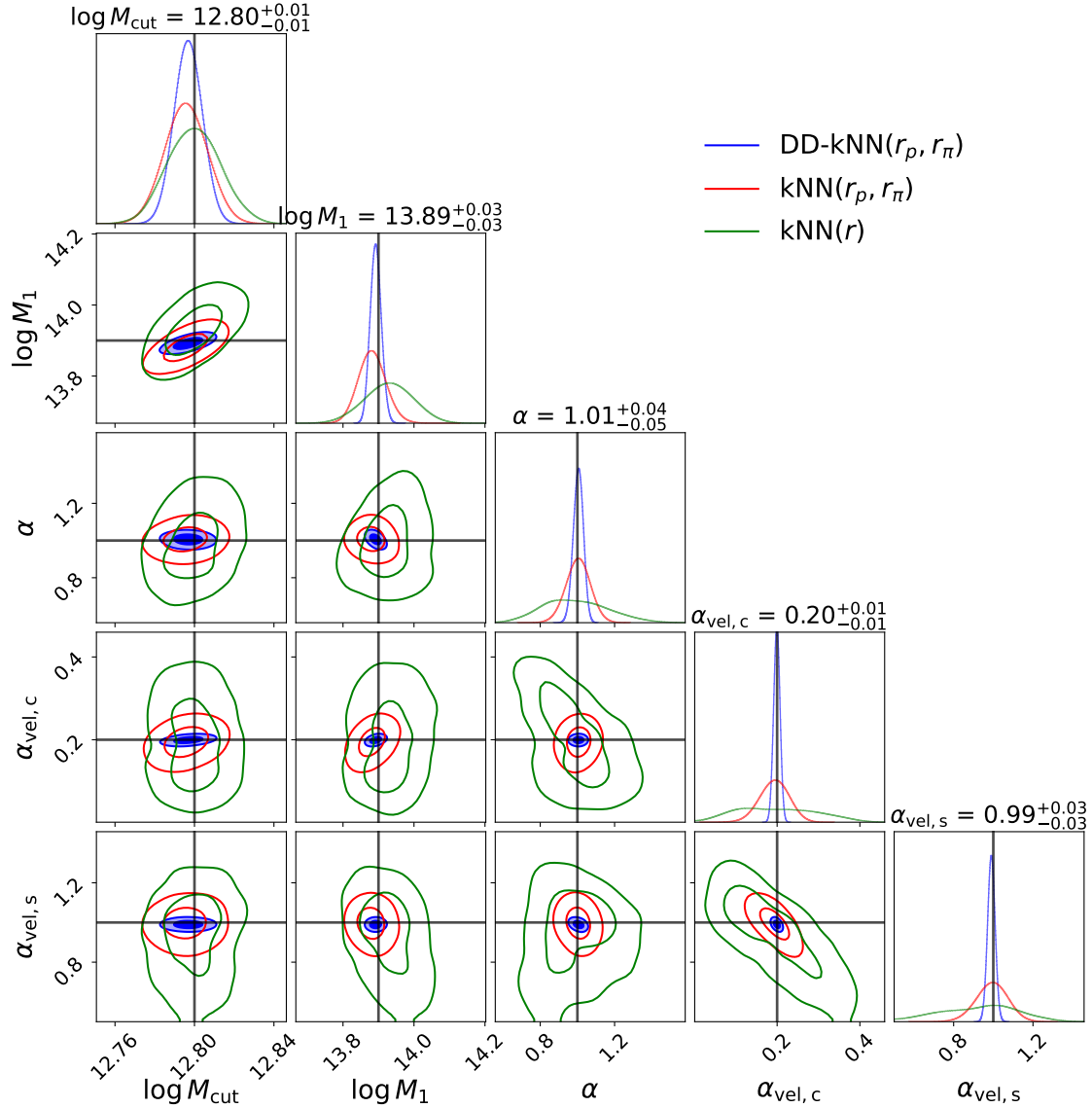


Figure 8. The HOD posterior recovery with 3 different flavors of k NNs. We only show the 1σ and 2σ contours. The black lines indicate the underlying truth. The marginalized constraints shown at the top of the 1D PDFs indicate the mean and the 2σ constraints of the DD- k NN(r_p, r_π) statistic. All three k NNs are tabulated from $k = 1$ to $k = 10$, with scale range $0.5\text{--}30h^{-1}\text{Mpc}$.

directions in the posterior contours is consistent with the theoretical notion that the k NN taps into the information content of higher order correlation functions, but without the computational complexities.

The fact that DD- k NN and k NN(r_p, r_π) have different degeneracies also suggests that the two statistics capture different features in the density field and that a joint analyses of these two statistics can be particularly fruitful. We leave that to future work as we do not have enough covariance realizations to confidently derive the joint covariance matrix between the two statistics.

We list the FoMs of the four statistics in Table 1. It is also helpful to think of them as inverses of the sample size needed to achieve the same model constraints. Of course, this is assuming that the constraining power is limited by sample variance, i.e. $\text{FoM} \sim 1/\sqrt{\text{Var}} \sim 1/\sqrt{N}$, where N is sample size. This suggests that to achieve the same level of constraints on the HOD, the 2PCF requires 4 times the sample size as that of DD- k NN. This is significant

given the high cost of modern surveys. Though it remains to be seen if such conclusions would extend to cosmological parameters.

These results clearly position the 2D k NNs as powerful tools in maximally capturing the information content of upcoming galaxy survey data across a wide range of scales. Specifically, DD- k NNs are highly sensitive probes of highly non-linear scales and should be particularly powerful in constraining and validating galaxy bias models. This also presents exciting opportunities in combining the 2D k NNs with other probes such as galaxy-galaxy lensing to break parameter degeneracies and test robustness of galaxy bias models. It could also be potentially interesting to combine traditional clustering probes with the query-data k NN(r_p, r_π) as it accesses a different set of information in the density field that were not accessible via traditional clustering statistics.

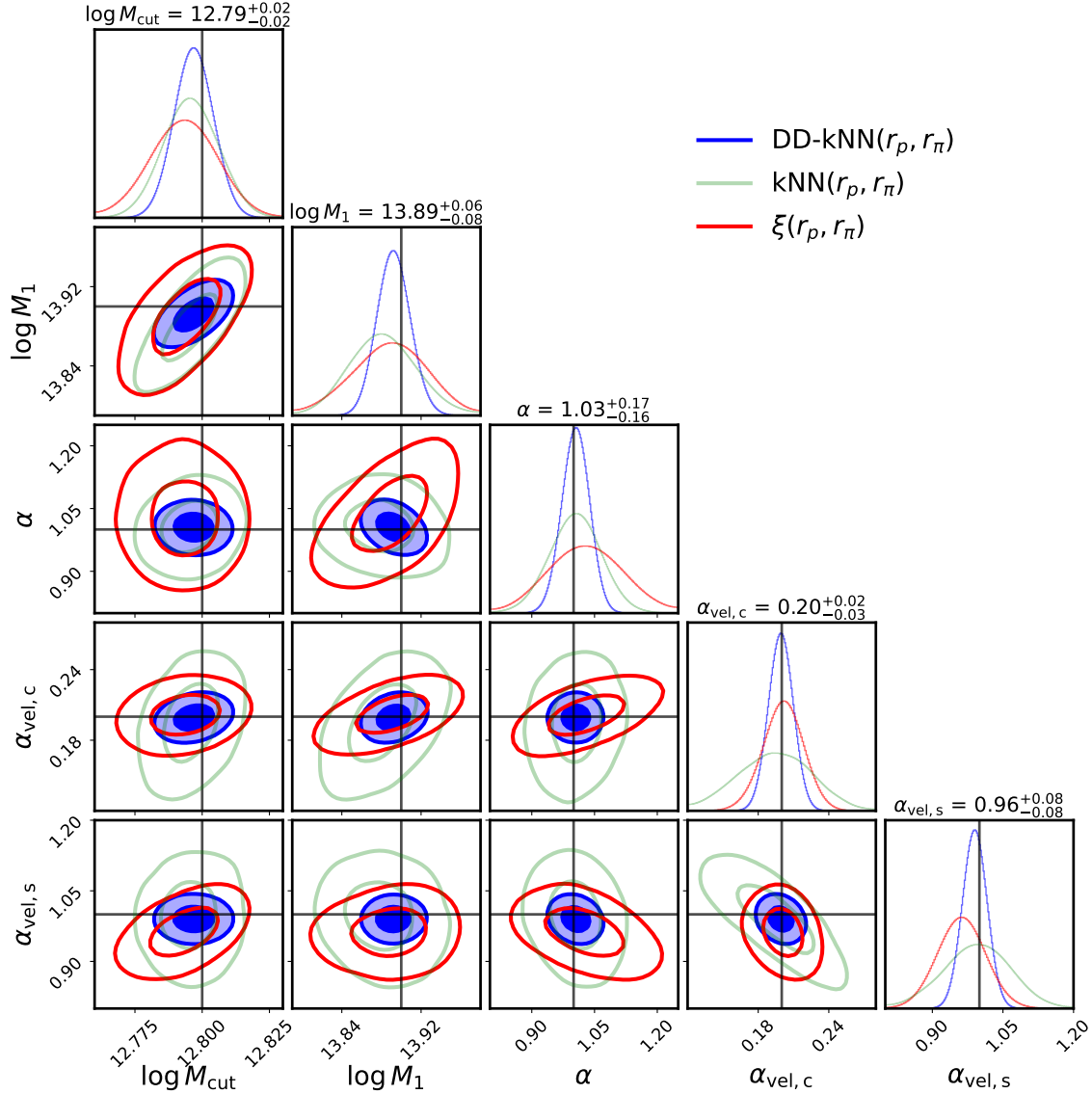


Figure 9. The HOD posterior recovery with the redshift-space 2PCF compared with the 2D kNNs. We show the 1 and 2σ contours. The black lines indicate the underlying truth. The marginalized constraints shown at the top of the 1D PDFs indicate the 2σ constraints of $\xi(r_p, r_\pi)$. We have highlighted the DD-kNN as it produces tighter constraints compared to the query-data kNN(r_p, r_π).

4.4 Galaxy assembly bias

A commonly explored and physically motivated extension to the standard HOD model is the so-called galaxy assembly bias, i.e. galaxy occupation correlates with secondary halo properties beyond just halo mass (e.g. Wechsler & Tinker 2018; Artale et al. 2018; Zehavi et al. 2018; Bose et al. 2019; Contreras et al. 2019; Hadzhiyska et al. 2020; Xu et al. 2021a; Hearin et al. 2016; Gao et al. 2005; Zentner et al. 2005; Zhu et al. 2006; Wechsler et al. 2006; Gao & White 2007; Croton et al. 2007; Li et al. 2008). Mathematically, it extends the standard HOD probability distribution $P(N_g|M_h)$ to $P(N_g|M_h, x)$, where N_g is the number of galaxies, M_h is the halo mass, and x is some secondary halo property. Galaxy assembly bias is important because it not only alters the interpretation of the underlying galaxy evolution models, but also significantly impacts galaxy clustering and ignoring it can bias cosmology constraints (Zentner et al. 2014; Pujol & Gaztañaga 2014; Lange et al. 2019). In this section, we

compare the constraining power of the 2D kNN statistics and the full-shape 2PCF on galaxy assembly bias.

Traditionally, galaxy concentration has been used as the secondary marker of galaxy secondary bias (also known as galaxy assembly bias) due to the concentration's correlation with halo age (e.g. Wechsler et al. 2002; Croton et al. 2007; Gao & White 2007), with older halos having higher concentrations and vice versa. However, a series of recent studies found local environment of the halo to be an excellent tracer of galaxy secondary bias based on hydrodynamical simulations and semi-analytic models (e.g. Yuan et al. 2022; Hadzhiyska et al. 2020; Xu et al. 2021a,b; Delgado et al. 2022). Thus, for this test, we adopt the environment-based assembly bias parameterization ($B_{\text{cent}}, B_{\text{sat}}$) as implemented in ABACUSHOD. Briefly, the environment is defined as the mass density within a $r_{\text{env}} = 5h^{-1}\text{Mpc}$ top-hat of the halo center, excluding the halo itself. $B_{\text{cent}} = 0, B_{\text{sat}} = 0$ indicate no environment-based secondary bias. A positive B indicates a preference for halos in less dense environments, and vice versa.

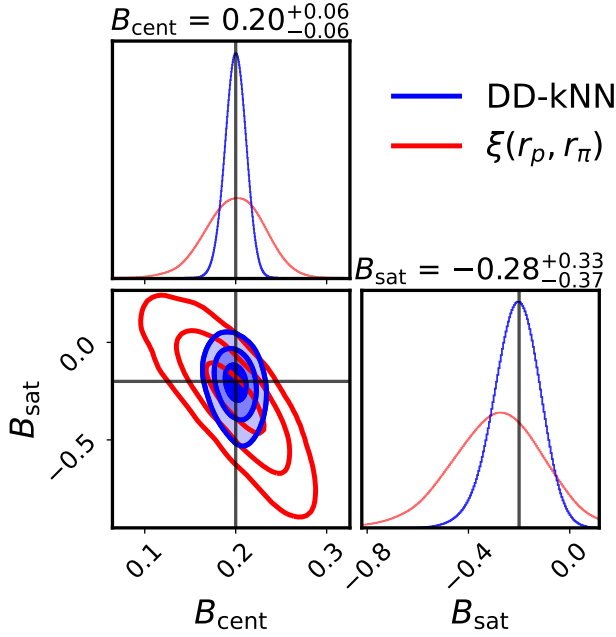


Figure 10. The marginalized recovery of galaxy assembly bias parameters B_{cent} and B_{sat} . The black lines indicate the truth values in the mock catalog. The blue and red contours indicate the $1 - 3\sigma$ constraints with the DD- k NN and $\xi(r_p, r_\pi)$, respectively. The titles show the 95% constraints with $\xi(r_p, r_\pi)$.

Parameter	truth	$\xi(r_p, r_\pi)$	DD- k NN(r_p, r_π)
B_{cent}	0.2	0.20 ± 0.06	0.20 ± 0.02
B_{sat}	-0.2	-0.28 ± 0.35	-0.21 ± 0.16

Table 2. The posterior constraints of the galaxy assembly bias parameters, using the redshift-space 2-point correlation function and the DD- k NN. The errorbars correspond to 95% uncertainties.

To evaluate the constraining power on B_{cent} and B_{sat} of our summary statistics, we follow the same procedure as described in section 4, but with a mock underlying HOD model that includes galaxy assembly bias, where $B_{\text{cent}} = 0.2$ and $B_{\text{sat}} = -0.2$. Physically, in this mock model the centrals prefer halos in denser environments whereas the satellites prefer halos in less dense environments. Figure 10 shows the marginalized posterior constraints on the two assembly bias parameters using the DD- k NN and the full shape 2PCF $\xi(r_p, r_\pi)$. We summarize the marginalized posterior constraints in Table 2. While both summary statistics recover unbiased constraints on the assembly bias parameters, the DD- k NN clearly derives 2-3 times tighter constraint along either parameter direction, further demonstrating the information content of the 2D k NN statistics.

5 DISCUSSIONS AND CONCLUSIONS

Beyond 2PCF statistics are needed to summarize the rich information on small scales in the era of precision galaxy clustering measurements enabled by DESI and other upcoming surveys. In this work, we introduce novel 2D generalizations of the k -th nearest neighbor statistics and use the lightcone-based forward model framework described in Yuan et al. (2023) to test the constraining power of these

statistics on the galaxy-halo connection model. We show that the 2D k NNs readily generate other popular galaxy clustering statistics such as counts-in-cells, void probability functions, and the 2-point correlation function. Moreover, we show that the 2D k NN are computationally efficient.

By conducting model recovery tests using the lightcone-based forward model, we find that the data-data 2D k NN formulation extracts the most galaxy-halo connection information among the variations. We compare the DD- k NN to the full-shape 2PCF $\xi(r_p, r_\pi)$ and find that the DD- k NN is a significantly stronger probe of essentially all aspects of the galaxy-halo connection model, including galaxy assembly bias. This is consistent with the theoretical notion that the k NNs encode not just the 2-point information, but also information from higher order n -point statistics. These tests also demonstrate the additional statistical power accessible on small scales through novel summary statistics. Our forecasts are also robust through the use of the lightcone-based forward model, exposing the summary statistics to the full range of observational systematics and survey realism.

The goal of developing these novel statistics is to be able to access and disentangle the galaxy-halo connection and cosmology information on non-linear scales. In the next paper, we will extend our model to include cosmology variations. So far, the tight constraints we get on M_{cut} at fixed cosmology suggests that the 2D k NNs tightly constrain the amplitude of galaxy clustering. This means that if we can break the degeneracies between galaxy bias and the amplitude of the matter power spectrum (for example by combining DD- k NN with galaxy-galaxy lensing), the 2D k NNs can prove to be a powerful probe of cosmology. This is particularly fruitful and timely as DESI and other survey facilities come online, which will produce high-density high-completeness samples particularly suited for small-scale analyses.

ACKNOWLEDGEMENTS

We would like to thank Risa Wechsler, Arka Banerjee, Ashley Ross, Sebastian Wagner-Carena, Philip Mansfield, and others for useful feedback and suggestions in various stages of this analysis.

This work was supported by U.S. Department of Energy through grant DE-SC0013718 and under DE-AC02-76SF00515 to SLAC National Accelerator Laboratory.

This work used resources of the National Energy Research Scientific Computing Center (NERSC), a U.S. Department of Energy Office of Science User Facility located at Lawrence Berkeley National Laboratory, operated under Contract No. DE-AC02-05CH11231.

The ABACUSUMMIT simulations were conducted at the Oak Ridge Leadership Computing Facility, which is a DOE Office of Science User Facility supported under Contract DE-AC05-00OR22725, through support from projects AST135 and AST145, the latter through the Department of Energy ALCC program.

DATA AVAILABILITY

The simulation data are available at <https://abacussummit.readthedocs.io/en/latest/>. The ABACUSHOD code package is publicly available as a part of the ABACUSUTILS package at <https://github.com/abacusorg/abacusutils>. Example usage can be found at <https://abacusutils.readthedocs.io/en/latest/hod.html>.

REFERENCES

- Artale M. C., Zehavi I., Contreras S., Norberg P., 2018, *MNRAS*, **480**, 3978
- Banerjee A., Abel T., 2021a, *MNRAS*, **500**, 5479
- Banerjee A., Abel T., 2021b, *MNRAS*, **504**, 2911
- Banerjee A., Kokron N., Abel T., 2022, *MNRAS*, **511**, 2765
- Bose S., Eisenstein D. J., Hernquist L., Pillepich A., Nelson D., Marinacci F., Springel V., Vogelsberger M., 2019, *MNRAS*, **490**, 5693
- Carron J., 2012, *Phys. Rev. Lett.*, **108**, 071301
- Contreras S., Zehavi I., Padilla N., Baugh C. M., Jiménez E., Lacerna I., 2019, *MNRAS*, **484**, 1133
- Croton D. J., Gao L., White S. D. M., 2007, *MNRAS*, **374**, 1303
- DESI Collaboration et al., 2016, arXiv e-prints, p. arXiv:1611.00036
- DeRose J., et al., 2019, *ApJ*, **875**, 69
- Delgado A. M., Wadekar D., Hadzhiyska B., Bose S., Hernquist L., Ho S., 2022, *MNRAS*, **515**, 2733
- Gao L., White S. D. M., 2007, *MNRAS*, **377**, L5
- Gao L., Springel V., White S. D. M., 2005, *MNRAS*, **363**, L66
- Garrison L. H., Eisenstein D. J., Pinto P. A., 2019, *MNRAS*, **485**, 3370
- Garrison L. H., Eisenstein D. J., Ferrer D., Maksimova N. A., Pinto P. A., 2021, *MNRAS*, **508**, 575
- Guo H., et al., 2015, *MNRAS*, **446**, 578
- Hadzhiyska B., Bose S., Eisenstein D., Hernquist L., Spergel D. N., 2020, *MNRAS*, **493**, 5506
- Hadzhiyska B., Eisenstein D., Bose S., Garrison L. H., Maksimova N., 2022a, *MNRAS*, **509**, 501
- Hadzhiyska B., Garrison L. H., Eisenstein D., Bose S., 2022b, *MNRAS*, **509**, 2194
- Hahn C., Villaescusa-Navarro F., Castorina E., Scoccimarro R., 2020, *J. Cosmology Astropart. Phys.*, **2020**, 040
- Hearin A. P., Zentner A. R., van den Bosch F. C., Campbell D., Tollerud E., 2016, *MNRAS*, **460**, 2552
- Ishiyama T., et al., 2021, *MNRAS*, **506**, 4210
- Ivezić Ž., et al., 2019, *ApJ*, **873**, 111
- Kwan J., Heitmann K., Habib S., Padmanabhan N., Lawrence E., Finkel H., Frontiere N., Pope A., 2015, *ApJ*, **810**, 35
- Landy S. D., Szalay A. S., 1993, *ApJ*, **412**, 64
- Lange J. U., van den Bosch F. C., Zentner A. R., Wang K., Hearin A. P., Guo H., 2019, *MNRAS*, **490**, 1870
- Laureijs R., et al., 2011, arXiv e-prints, p. arXiv:1110.3193
- Levi M., et al., 2013, arXiv e-prints, p. arXiv:1308.0847
- Li Y., Mo H. J., Gao L., 2008, *MNRAS*, **389**, 1419
- Maksimova N. A., Garrison L. H., Eisenstein D. J., Hadzhiyska B., Bose S., Satterthwaite T. P., 2021, *MNRAS*,
- Paillas E., et al., 2023, *MNRAS*,
- Peebles P. J. E., 1980, The large-scale structure of the universe
- Pujol A., Gaztañaga E., 2014, *MNRAS*, **442**, 1930
- Sinha M., Garrison L. H., 2020, *MNRAS*, **491**, 3022
- Slepian Z., et al., 2017, *MNRAS*, **468**, 1070
- Speagle J. S., 2020, *MNRAS*, **493**, 3132
- Speagle J., Barbary K., 2018, dynesty: Dynamic Nested Sampling package, Astrophysics Source Code Library (ascl:1809.013)
- Takada M., Jain B., 2003, *MNRAS*, **340**, 580
- Takada M., et al., 2014, *PASJ*, **66**, R1
- Uhlemann C., Friedrich O., Villaescusa-Navarro F., Banerjee A., Codis S., 2020, *MNRAS*, **495**, 4006
- Valogiannis G., Dvorkin C., 2022, *Phys. Rev. D*, **105**, 103534
- Wang Y., Banerjee A., Abel T., 2022, *MNRAS*, **514**, 3828
- Wechsler R. H., Tinker J. L., 2018, *ARA&A*, **56**, 435
- Wechsler R. H., Bullock J. S., Primack J. R., Kravtsov A. V., Dekel A., 2002, *ApJ*, **568**, 52
- Wechsler R. H., Zentner A. R., Bullock J. S., Kravtsov A. V., Allgood B., 2006, *ApJ*, **652**, 71
- White S. D. M., 1979, *MNRAS*, **186**, 145
- Xu X., Zehavi I., Contreras S., 2021a, *MNRAS*, **502**, 3242
- Xu X., Kumar S., Zehavi I., Contreras S., 2021b, *MNRAS*, **507**, 4879
- Ye J.-N., Guo H., Zheng Z., Zehavi I., 2017, *ApJ*, **841**, 45
- Yuan S., Eisenstein D. J., Garrison L. H., 2017, *MNRAS*, **472**, 577
- Yuan S., Garrison L. H., Hadzhiyska B., Bose S., Eisenstein D. J., 2021, *MNRAS*, **510**, 3301
- Yuan S., Hadzhiyska B., Bose S., Eisenstein D. J., 2022, *MNRAS*, **512**, 5793
- Yuan S., Hadzhiyska B., Abel T., 2023, *MNRAS*, **520**, 6283
- Zehavi I., Contreras S., Padilla N., Smith N. J., Baugh C. M., Norberg P., 2018, *ApJ*, **853**, 84
- Zentner A. R., Berlind A. A., Bullock J. S., Kravtsov A. V., Wechsler R. H., 2005, *ApJ*, **624**, 505
- Zentner A. R., Hearin A. P., van den Bosch F. C., 2014, *MNRAS*, **443**, 3044
- Zheng Z., et al., 2005, *ApJ*, **633**, 791
- Zheng Z., Coil A. L., Zehavi I., 2007, *ApJ*, **667**, 760
- Zhu G., Zheng Z., Lin W. P., Jing Y. P., Kang X., Gao L., 2006, *ApJ*, **639**, L5

This paper has been typeset from a \LaTeX file prepared by the author.